Band structures and skin effects of coupled nonreciprocal Su-Schrieffer-Heeger lattices

Jia-Rui Li,[1] Chao Luo,[1] Lian-Lian Zhang,[1,*] Shu-Feng Zhang,[2] Pan-Pan Zhu,[1] and Wei-Jiang Gong [1,†]

[1]*College of Sciences, Northeastern University, Shenyang 110819, China*
[2]*School of Physics and Technology, University of Jinan, Jinan 250022, China*

We pay attention to the influences of the nonreciprocal coupling on the band structures and skin effects in the coupled Su-Schrieffer-Heeger (SSH) lattices. It is shown that the nonreciprocal coupling leads to the non-Hermitian skin effect in a substantial way. Besides, it widens the parameter space of the zero-energy modes in the band gap, and modifies the transition manner from the topologically trivial to topologically nontrivial phase. When the nonreciprocal coupling exceeds its critical value, the zero-energy modes will split, giving rise to the appearance of new nonzero- or complex-energy modes. What is more, differently from the chain configuration, the nonreciprocal coupling makes purely imaginary energy modes emerge in the band gap of the SSH-ring configuration. Next in the presence of hopping disorder, we observe that the zero-energy modes are relatively robust, whereas the imaginary part of energies displays the nonmonotonic changes. It can be thus believed that all these findings promote understanding the influences of nonreciprocal couplings on the types and properties of isolated modes in the SSH lattices.

I. INTRODUCTION

The fundamental assumption of quantum mechanics is that all physical observations must be represented by the Hermitian operators in the Hilbert space [1–4], which leads to real energy eigenvalues and guarantees conservation of probability. This shows that as a Hamiltonian operator ($H = H^\dagger$) to describe the physical system, its Hermitian property can ensure that the energy is real. For non-Hermitian Hamiltonians, since this condition is not satisfied, its energy is complex. However, in 1998 Bender and Boettcher found that non-Hermitian systems can still possess completely real energy spectra, i.e., non-Hermitian operators with parity-time ($\mathcal{PT}$) reversal symmetry [5–7]. As the theory was put forward, non-Hermitian Hamiltonians with $\mathcal{PT}$ symmetry have been one of the hot topics in quantum physics. The researchers tried to introduce $\mathcal{PT}$-symmetric imaginary potentials with gain and loss into topological systems, and observed the occurrence of new phenomena in various structures, such as the one-dimensional (1D) Su-Schrieffer-Heeger (SSH) chain, Kitaev model, trimer lattice, graphene, and two-dimensional (2D) SSH lattice [8–18]. On the experimental side, $\mathcal{PT}$ symmetry can be simulated by various physical systems. As a typical case, the $\mathcal{PT}$-symmetric systems can be achieved in optical [19,20] and topological photonic systems [21–23]. With the deepening of research, $\mathcal{PT}$ symmetry has also been applied in many fields, such as single-mode lasing action in $\mathcal{PT}$-symmetric microcavity arrangements [24], perfect cavity absorber lasers [25,26], and metamaterials with extraordinary properties [27,28].

During the development of non-Hermitian research, it has been found that in 1D systems, eigenstates with open boundary conditions are localized near the boundary of the system in the form of exponential decay, which is called the non-Hermitian skin effect [29–33]. The appearance of this phenomenon indicates that the open boundary spectrum of the system is different from the periodic boundary spectrum, and the bulk-boundary correspondence of the system completely collapses [29,34,35]. Due to the breaking of the bulk-boundary correspondence, it is not feasible to use topological invariants under periodic boundary conditions to describe the topological properties of such systems. Therefore, Wang *et al.* proposed the non-Bloch energy band theory in 2019 [29]. The proposal of this theory is to expand the application range of energy band theory. Subsequently, concepts have been proposed and used, such as the generalized Brillouin zone (GBZ) [36–38], non-Bloch bulk-boundary correspondence [29], and non-Bloch topological invariants [29,36]. With the continuous advances of the theory, the development of experiment has been promoted. At present, the non-Hermitian skin effect and non-Bloch energy band theory have been realized and applied experimentally, including cold atoms, quantum optical systems, and optical grid systems [39–42]. More recently, Helbig *et al.* have reported the experimental observation of the bulk-boundary correspondence (BBC) violation, i.e., non-Hermitian skin effect, by constructing a nonreciprocal SSH topolectrical circuit [43].

The great progresses in experiment inspire us to think of more interesting phenomena by designing SSH-derived structures. In this work we study the coupled nonreciprocal SSH lattice by introducing the nonreciprocal coupling parameter γ. Our purpose is to clarify its influences on the band variations. And then, after performing calculation on the chain and ring configurations, we observe that the nonreciprocal coupling

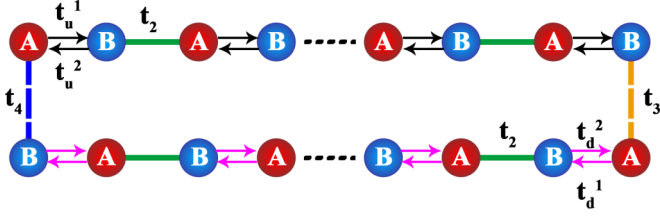*zhanglianlian@mail.neu.edu.cn
†gwj@mail.neu.edu.cn

FIG. 1. Schematic diagram of the coupled nonreciprocal Su-Schrieffer-Heeger (SSH) lattice. The red and blue circles represent the sublattices A and B. The black and pink arrows denote the intracell hopping terms $t_u^{1(2)}$ and $t_d^{1(2)}$ in the upper and lower branches. The green (single) line is the intercell hopping term t_2, and the yellow and blue (dashed) lines are the coupling coefficients between the two branches.

leads to the non-Hermitian skin effect in a substantial way, and widens the parameter space of the zero-energy modes, which are accompanied by the modification of the topological phase transition manner. As a typical case, when the nonreciprocal coupling exceeds its critical value, the zero-energy modes will split, leading to the appearance of new nonzero modes or complex-energy states in the band gap. Moreover, differently from the chain configuration, the nonreciprocal coupling makes purely imaginary energy modes emerge in the band gap of the SSH-ring configuration. In addition, when the intercell-hopping disorder is taken into account, it is shown that the zero-energy modes are robust for the case of weak disorder, whereas the imaginary part of energies displays the nonmonotonic changes in this process. All these results can be helpful in understanding the band structures and respective states in the nonreciprocal SSH lattices.

II. THEORETICAL MODEL

The general structure of the 1D coupled nonreciprocal SSH lattice that we consider is illustrated in Fig. 1. As shown in this figure, each unit cell hosts two distinct sites, denoted as A and B (i.e, the blue and red dots). The Hamiltonian of such a coupled nonreciprocal SSH lattice can be written as

$$H = H_u + H_d + H_{ud}. \tag{1}$$

The first and second terms, i.e., H_u and H_d, are the Hamiltonians of the upper and lower branches, which are taken as

$$H_u = \sum_{n=1}^{N_u} \left(t_u^1 c_{A,n}^\dagger c_{B,n} + t_u^2 c_{B,n}^\dagger c_{A,n} \right)$$
$$+ \sum_{n=1}^{N_u-1} \left(t_2 c_{B,n}^\dagger c_{A,n+1} + \text{H.c.} \right),$$

$$H_d = \sum_{n=1}^{N_d} \left(t_d^1 c_{A,n}^\dagger c_{B,n} + t_d^2 c_{B,n}^\dagger c_{A,n} \right)$$
$$+ \sum_{n=1}^{N_d-1} \left(t_2 c_{B,n}^\dagger c_{A,n+1} + \text{H.c.} \right). \tag{2}$$

$c_{\alpha,n}^\dagger$ ($c_{\alpha,n}$) is the creation (annihilation) operator at site α of the nth unit cell in each part of the SSH lattice ($\alpha = A, B$). N_u is

the number of unit cells in the upper branch, and N_d is the unit-cell number in the lower branch. $t_u^{1(2)} = t_u + t_0 e^{\mp\gamma}$ represents the intersite hopping in the upper branch, whereas $t_d^{1(2)} = t_d + t_0 e^{\mp\gamma}$ corresponds to the intersite hopping in the lower branch. Besides, t_2 describes the intercell hopping coefficient, and γ denotes the nonreciprocal strength. It is evident that when $\gamma = 0$, the Hamiltonian describes the Hermitian SSH chain.

The third term H_{ud} corresponds to the coupling between the two branches of the SSH lattice, which is given as

$$H_{ud} = t_3 c_{B,N_u}^\dagger c_{A,N_u+1} + t_4 c_{B,N_u+N_d}^\dagger c_{A,1} + \text{H.c.} \tag{3}$$

t_3 and t_4 are the coupling coefficients between the two branches. When only t_4 is taken to be zero, this system transforms into the chain configuration. Instead, when both t_3 and t_4 are not equal to zero, it exactly describes the ring configuration. In terms of parameter settings, we would like to take t_u, t_d, t_2, t_3, t_4, and γ to be the real numbers.

According to the Hamiltonian expressions above, we are allowed to write out the matrix form of the Hamiltonian in the real space, i.e., $H = \Psi^\dagger H_r \Psi$, including

$$H_r = \begin{bmatrix} H_u & H_{ud} \\ H_{ud}^* & H_d \end{bmatrix}, \tag{4}$$

and $\Psi = (\Psi_u, \Psi_d)^T$, where $\Psi_u = (\psi_{a,1}, \psi_{b,1}, \ldots, \psi_{a,N_u}, \psi_{b,N_u})$ and $\Psi_d = (\psi_{a,N_u+1}, \psi_{b,N_u+1}, \ldots, \psi_{a,N_u+N_d}, \psi_{b,N_u+N_d})$. For the elements of H_r, they can be expressed as

$$H_{\alpha\in u,d} = \begin{bmatrix} 0 & t_\alpha^1 & 0 & 0 & \cdots \\ t_\alpha^2 & 0 & t_2 & 0 & \cdots \\ 0 & t_2 & 0 & t_\alpha^1 & \cdots \\ 0 & 0 & t_\alpha^2 & 0 & \cdots \\ \vdots & \vdots & \vdots & \vdots & \ddots \end{bmatrix}_{2N_\alpha \times 2N_\alpha},$$

$$H_{ud} = \begin{bmatrix} 0 & \cdots & \cdots & t_4 \\ \vdots & \ddots & \ddots & 0 \\ 0 & \ddots & \ddots & \vdots \\ t_3 & \cdots & \cdots & 0 \end{bmatrix}_{2N_u \times 2N_d}. \tag{5}$$

Based on the previous works [37,38,44], we can calculate the eigenenergy equation and the conditions of topological phase transition in our structure. First of all, we calculate the bulk band eigenenergy equation. The eigenenergy and wave function expressions in the real space can be obtained by solving the Schrödinger equation $H|\Psi\rangle = E|\Psi\rangle$ in which $|\Psi\rangle = \sum_{n=1}^{N_u+N_d} (\psi_{a,n} c_{A,n}^\dagger + \psi_{b,n} c_{B,n}^\dagger)|0\rangle$. $\psi_{a(b),n}$ is the wave function of sublattice A (B). This equation consists of a series of equations, including the bulk-state equations

$$t_\alpha^1 \psi_{b,n} + t_2 \psi_{b,n-1} = E \psi_{a,n},$$
$$t_\alpha^2 \psi_{a,n} + t_2 \psi_{a,n+1} = E \psi_{b,n}. \tag{6}$$

For $n \in [1, N_u]$, the t_α^1 and t_α^2 can be written as $t_u^1 = t_u + t_0 e^{-\gamma}$ and $t_u^2 = t_u + t_0 e^\gamma$. For $n \in [N_u + 1, N_u + N_d]$, $t_\alpha^1(t_\alpha^2)$ is $t_d^1 = t_d + t_0 e^{-\gamma}$ ($t_d^2 = t_d + t_0 e^\gamma$). In this equation, $\psi_{a,n}$ and $\psi_{b,n}$ are decoupled from each other. For the bulk band wave functions, we take an ansatz as a linear combination:

$$\psi_{v,n} = \begin{cases} \sum_j \beta_{u,j}^n \phi_v^{(j)}, & n \in [1, N_u], \\ \sum_j \beta_{d,j}^{n-N_u} \varphi_v^{(j)}, & n \in [N_u + 1, N_u + N_d], \end{cases} \tag{7}$$

where $\upsilon = A, B$. By substituting Eq. (7) into Eq. (6), the bulk eigenequation can be obtained:

$$
\begin{aligned}
\left(t_\alpha^1 + t_2 \beta_{\alpha,j}^{-1}\right)\phi_B^{(j)}\big(\varphi_B^{(j)}\big) &= E\phi_A^{(j)}\big(\varphi_A^{(j)}\big), \\
\left(t_\alpha^2 + t_2 \beta_{\alpha,j}\right)\phi_A^{(j)}\big(\varphi_A^{(j)}\big) &= E\phi_B^{(j)}\big(\varphi_B^{(j)}\big).
\end{aligned} \tag{8}
$$

In nonreciprocal systems, we know that the eigenenergy equation of non-Bloch Hamiltonian $H(\beta)$ is written as $H(\beta)|\tilde{\Psi}\rangle = E|\tilde{\Psi}\rangle$. According to the above equation, we set $|\tilde{\Psi}\rangle = (\phi_A^{(j)}, \phi_B^{(j)})^T = (\varphi_A^{(j)}, \varphi_B^{(j)})^T$. Thus, we obtain the matrix form of $H(\beta_{\alpha,j})$ as

$$
H(\beta_{\alpha,j}) = \begin{bmatrix} 0 & t_\alpha^1 + t_2 \beta_{\alpha,j}^{-1} \\ t_\alpha^1 + t_2 \beta_{\alpha,j} & 0 \end{bmatrix}. \tag{9}
$$

$\beta_{\alpha,j}$ is the solution of the equation $\det[H(\beta_{\alpha,j}) - E] = 0$. Therefore, the eigenenergy equation can be written as

$$
\begin{aligned}
&t_2(t_\alpha + t_0 e^{-\gamma})\beta_{\alpha,j} + t_2(t_\alpha + t_0 e^{\gamma})\frac{1}{\beta_{\alpha,j}} \\
&+ \left[t_\alpha^2 + 2t_\alpha t_0 \cosh(\gamma) + t_0^2 + t_2^2 - E^2\right] = 0.
\end{aligned} \tag{10}
$$

From Eq. (10), we find that the eigenenergy equation is the quadratic equation of β. This means that the upper and lower branches have two solutions, i.e., $\beta_{u,1}$ ($\beta_{u,2}$) and $\beta_{d,1}$ ($\beta_{d,2}$). Also, we are allowed to get the relationship of the two solutions as $\beta_{\alpha,1}\beta_{\alpha,2} = \frac{t_\alpha + t_0 e^\gamma}{t_\alpha + t_0 e^{-\gamma}}$.

Next, we calculate the case of the boundary condition. Equation (7) should be suitable for the boundary conditions,

and when they are brought into the Schrödinger equation at the boundary, the nonzero solution of $\beta_{\alpha,j}$ can be figured out. The boundary conditions are exactly the domain wall boundary conditions, so the expressions of the boundary equation are

$$
t_u^1 \psi_{b,1} + t_4 \psi_{b,N_u+N_d} = E\psi_{a,1}, \tag{11}
$$

$$
t_u^2 \psi_{a,N_u} + t_3 \psi_{a,N_u+1} = E\psi_{b,N_u}, \tag{12}
$$

$$
t_d^1 \psi_{b,N_u+1} + t_3 \psi_{b,N_u} = E\psi_{a,N_u+1}, \tag{13}
$$

$$
t_d^2 \psi_{a,N_u+N_d} + t_4 \psi_{a,1} = E\psi_{b,N_u+N_d}. \tag{14}
$$

Substituting the general solution of Eq. (7) when $j = 1, 2$ into Eqs. (11)–(14), we get the four linear equations, that is,

$$
-t_2\phi_b^1 - t_2\phi_b^2 + t_4\beta_{d,1}^{N_d}\varphi_b^1 + t_4\beta_{d,2}^{N_d}\varphi_b^2 = 0, \tag{15}
$$

$$
-t_2\beta_{u,1}^{N_u+1}f_1\phi_b^1 - t_2\beta_{u,2}^{N_u+1}f_2\phi_b^2 + t_3\beta_{d,1}g_1\varphi_b^1 + t_3\beta_{d,2}g_2\varphi_b^2 = 0, \tag{16}
$$

$$
t_3\beta_{u,1}^{N_u}\phi_b^1 + t_3\beta_{u,2}^{N_u}\phi_b^2 - t_2\varphi_b^1 - t_2\varphi_b^2 = 0, \tag{17}
$$

$$
t_4f_1\beta_{u,1}\phi_b^1 + t_4f_2\beta_{u,2}\phi_b^2 - t_2g_1\beta_{d,1}^{N_d+1}\varphi_b^1 - t_2g_2\beta_{d,2}^{N_d+1}\varphi_b^2 = 0. \tag{18}
$$

Thus, the condition for the linear equation to have nontrivial solutions is written as $H_C\Phi = 0$, where $\Phi = (\phi_b^1, \phi_b^2, \varphi_b^1, \varphi_b^2)^T$ and

$$
H_C = \begin{bmatrix} -t_2 & -t_2 & t_4\beta_{d,1}^{N_d} & t_4\beta_{d,2}^{N_d} \\ -t_2\beta_{u,1}^{N_u+1}f_1 & -t_2\beta_{L,2}^{N_u+1}f_2 & t_3\beta_{d,1}g_1 & t_3\beta_{d,2}g_2 \\ t_3\beta_{u,1}^{N_u} & t_3\beta_{u,2}^{N_u} & -t_2 & -t_2 \\ t_4f_1\beta_{u,1} & t_4f_2\beta_{u,2} & -t_2g_1\beta_{d,1}^{N_d+1} & -t_2g_2\beta_{d,2}^{N_d+1} \end{bmatrix}. \tag{19}
$$

In these equations, $f_{1(2)} = \frac{\phi_a^j}{\phi_b^j}$ and $g_{1(2)} = \frac{\varphi_a^j}{\varphi_b^n}$ are the coefficients calculated from Eq. (8). The specific expressions are

$$
f_j = \frac{(t_u + t_0 e^{-\gamma})\beta_{u,j} + t_2}{E\beta_{u,j}} = \frac{E}{(t_u + t_0 e^\gamma) + t_2\beta_{u,j}}, \tag{20}
$$

$$
g_j = \frac{(t_d + t_0 e^{-\gamma})\beta_{d,j} + t_2}{E\beta_{d,j}} = \frac{E}{(t_d + t_0 e^\gamma) + t_2\beta_{d,j}}. \tag{21}
$$

By calculating $\det[H_C] = 0$, we obtain the relationship of the four solutions $\beta_{\alpha,j}$. In the situation of $N \to \infty$ and $E \to 0$, one can figure out the topological phase transition conditions in the generalized Brillouin zone. On the one hand, in the chain configuration where $t_2 = t_3$ and $t_4 = 0$ with $\gamma \neq 0$, the topological phase transition conditions are respectively

$$
t_u = \begin{cases} -t_0\cosh(\gamma) - \sqrt{t_2^2\cosh^2(\gamma) - t_0^2}, \\ t_2^2/(t_d + t_0 e^\gamma) - t_0 e^\gamma, \\ t_d - 2t_0\sinh(\gamma), \\ (t_2^2 - t_d t_0 e^{-\gamma} - t_0^2)/(t_d + t_0 e^\gamma). \end{cases} \tag{22}
$$

On the other hand, in the ring configuration with $t_2 = t_3 = t_4$ and $\gamma \neq 0$, the topological phase transition conditions change

to be

$$
t_u = \begin{cases} (t_2^2 - t_d t_0 e^\gamma - t_0^2)/(t_d + t_0 e^{-\gamma}), \\ (t_2^2 - t_d t_0 e^\gamma - t_0^2 e^{-2\gamma})/(t_d + t_0 e^{-\gamma}), \\ (t_2^2 - t_d t_0 e^\gamma - t_0^2 e^{2\gamma})/(t_d + t_0 e^\gamma), \\ -t_0\cosh(\gamma) - \sqrt{t_2^2\cosh^2(\gamma) - t_0^2}. \end{cases} \tag{23}
$$

One can surely judge the conditions of band closing according to the properties of $\beta_{\alpha,j}$. Now, from the phase transition conditions, we can readily observe that such two configurations have different topological phase transition conditions.

Following the analysis of the phase transition conditions, we would like to investigate the topological properties of this system by judging the Hamiltonian symmetry. In Kawabata's and Gong's works [45,46], they provide the symmetry classes in non-Hermitian systems. Therefore, we can clarify the symmetry in the real space from the expression of H_r. First, for the chain configuration with $t_2 = t_3$ and $t_4 = 0$, it only satisfies the particle-hole symmetry (PHS†) and sublattice symmetry (SLS), which are described as $\mathcal{C}H_r^*\mathcal{C}^{-1} = -H_r$ and $\mathcal{S}H_r\mathcal{S}^{-1} = -H_r$, respectively. Operators PHS† and SLS are both defined as $\mathcal{C}(\mathcal{S}) = I_{N_u+N_d} \otimes \sigma_z$, in which σ_z is the

z component of the Pauli matrix, and I is the unit matrix. Thus in this case, the system belongs to the D† class. Second, regarding the ring configuration when $t_2 = t_3 = t_4$, such a system turns out to be of the time-reversal symmetry TRS†, i.e., $\mathcal{T}H_r^T\mathcal{T} = H_r$. Here the operator $\mathcal{T}$ is written as $\mathcal{T} = I_2 \otimes \text{off-diag}(1, 1, 1, \ldots, 1)_{2N_u}$, in which

$$\text{off-diag}(1, 1, 1, \ldots, 1)_{2N_u} = \begin{pmatrix} 0 & \cdots & 0 & 1 \\ 0 & \cdots & 1 & 0 \\ 0 & \cdot^{\cdot^{\cdot}} & 0 & 0 \\ 1 & \cdots & 0 & 0 \end{pmatrix}_{2N_u * 2N_u}.$$

In addition to the above results, one can find that the ring configuration has the particle-hole symmetry (PHS†), i.e., $\mathcal{C}H_r^*\mathcal{C}^{-1} = -H_r$ with $\mathcal{C} = I_{N_u+N_d} \otimes \sigma_z$. Meanwhile, it satisfies the chiral symmetry, i.e., $\Gamma H_r^\dagger \Gamma^{-1} = -H_r$ in which $\Gamma = I_2 \otimes \text{off-diag}(-1, 1, -1, \ldots, 1)_{2N_u}$. Therefore, the ring configuration can be found to belong to the BDI† class. By calculation, it can be ascertained that the real part of eigenenergies is not equal to zero except the phase transition points, and the system has its real-line gap. Now with help of the above analysis and the conclusion in the previous works, we know that the system has the $\mathcal{Z}_2$ and $\mathcal{Z}$ class topological invariants in the chain and ring configurations, respectively.

III. NUMERICAL RESULTS AND DISCUSSION

Based on the theoretical deduction in Sec. II, we proceed to calculate the band structures of two configurations of the coupled nonreciprocal SSH lattice, namely, the chain configuration where $t_3 \neq 0$ and $t_4 = 0$ and the ring configuration ($t_3 \neq 0$ and $t_4 \neq 0$). To carry out numerical calculation, we take $t_0 = 1.0$ in this context. Namely, all the parameters that describe intersite couplings are in units of t_0 in this work.

Before our discussion, we would like to present the eigenenergy spectra of the single non-Hermitian SSH chain, as shown in Fig. 2. The specific derivation is depicted in the Appendix. It can be found that even in the presence of nonreciprocal factors, the system undergoes the process of gap closure and reopening with the increase of $\tilde{t}$ ($\tilde{t}$ is related to the intracell hopping). Namely, the transition points occur at $\tilde{t} = -2.09$ and $\tilde{t} = 0$, respectively. Between these two transition points, zero-energy modes come up. For the imaginary part of energy, it appears in the region of $-1.35 < \tilde{t} < -0.74$. The numerical results are consistent with the theoretical derivation. Figure 2(c) shows the $\tilde{t}$-$|\beta|$ curves under the condition of $\gamma = 0.3$ and $t_2 = 1.0$. The blue (solid) and green (dashed) lines represent $|\beta_1|$ and $|\beta_2|$, respectively. We find that the system obeys the relationship of $|\beta_1| = |\beta_2| = r$; i.e., $|\beta_1|$ and $|\beta_2|$ meet at $\tilde{t} = -2.09$ and $\tilde{t} = 0$. This result is quite consistent with the band-closing points in Fig. 2(a). In Fig. 2(d), we plot the probability density spectrum. It can be found that the bulk states are mainly located on the left side of the chain, and they are gradually suppressed to the center of the chain. For the zero-energy modes, they are localized seriously at $j = 1$. All these results should be attributed to the non-Hermitian skin effect.
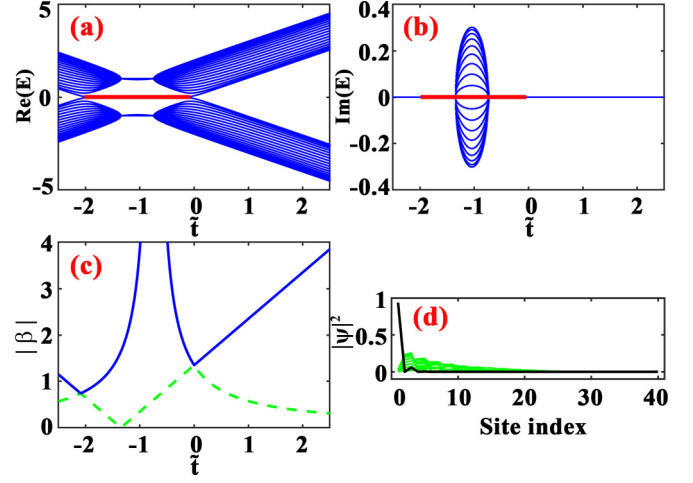

FIG. 2. (a), (b) Real and imaginary parts of the eigenenergies of the single non-Hermitian SSH chain, under the condition of $\gamma = 0.3$. Other parameters are taken to be $N = 20$ and $t_2 = 1.0$. Red (bold) lines describe the zero mode. (c) $\tilde{t}$-$|\beta|$ curves in the case of $\gamma = 0.3$ and $t_2 = 1.0$. The blue (solid) and green (dashed) lines represent $|\beta_1|$ and $|\beta_2|$. (d) The probability density spectra in the case of $\tilde{t} = -1.1$.

A. Chain configuration ($t_3 \neq 0$ and $t_4 = 0$)

We start by discussing the energy band characteristics of the chain configuration. Figure 3 plots the real and imaginary parts of energy bands under the condition of $N_u = N_d = 20$.
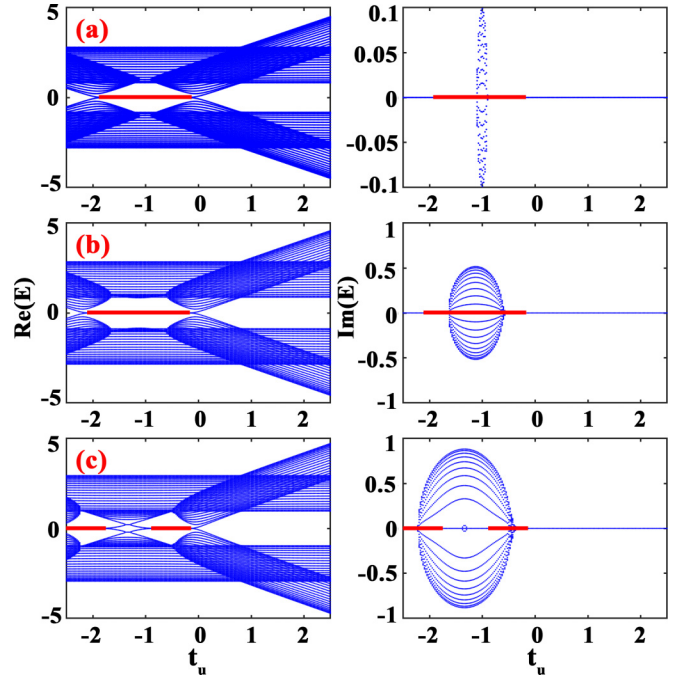

FIG. 3. Energy spectra of the chain configuration with the change of t_u, where (a) $\gamma = 0.1$, (b) $\gamma = 0.5$, and (c) $\gamma = 0.8$. The left column is the real part of the eigenenergies, and the right column is the corresponding imaginary part. The red (bold) lines represent the real and imaginary parts of the zero-energy modes. The other parameters are set as $N_u = N_d = 20$, $t_2 = t_3 = 1.0$, $t_d = 0.8$, and $t_4 = 0$.
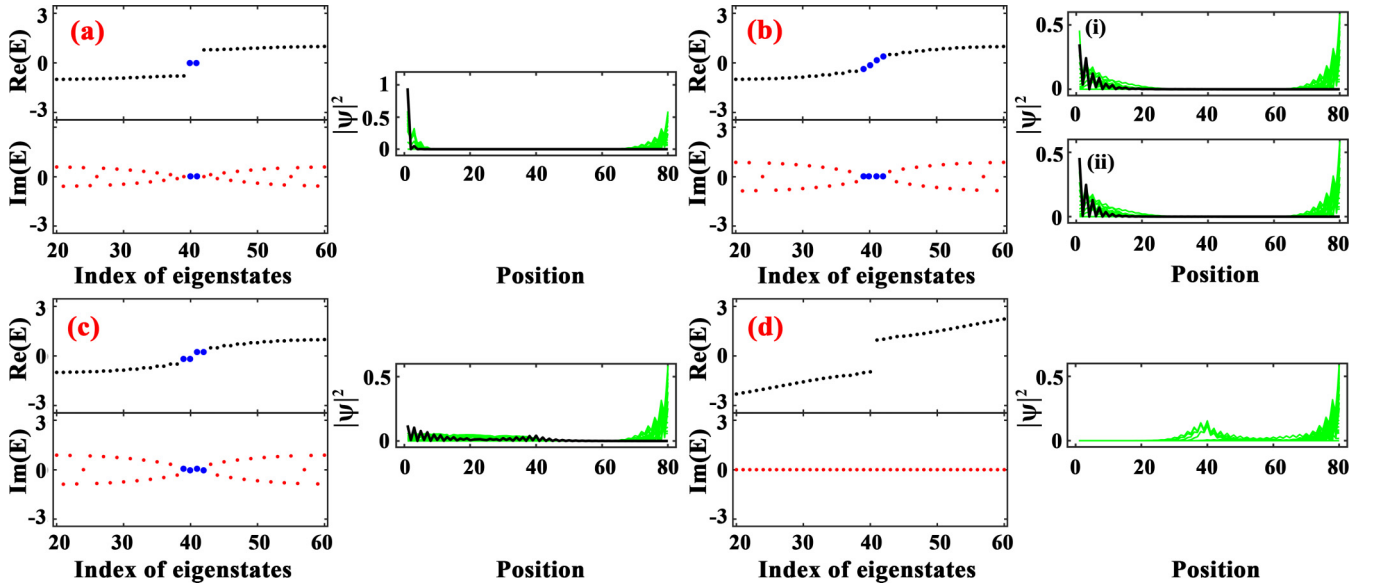
FIG. 4. Eigenenergy spectra and probability density spectra. The parameters are set as (a) $t_u = -2.0$, (b) $t_u = -1.5$, (c) $t_u = -1.35$, (d) $t_u = 1.0$. The black (bold) lines represent the probability distribution of the zero-energy modes or nonzero-energy modes produced after splitting, and the green lines describe the probability distribution of the bulk states. Other parameters are set as $N_u = N_d = 20$, $t_d = 0.8$, $\gamma = 0.8$, and $t_2 = t_3 = 1.0$.

From the spectra of the real and imaginary parts of energy, one can find that γ has different regulatory effects on the bulk states and zero-energy modes of this system. As shown in Fig. 3(a) where $\gamma = 0.1$, the energy gap is closed at the points $t_u = -1.95$ and $t_u = -0.25$, respectively, and zero-energy modes come up between these two critical points (illustrated by the red line). From the spectrum of the imaginary part of the energy, it can be observed that the imaginary part appears in the range of $t_u \in [-1.1, -0.9]$. This indicates that the nonreciprocal coupling induces the appearance of complex eigenvalues in the bulk states. Alternatively, the imaginary part of the zero-energy modes is always equal to zero, which means that the eigenenergies of the zero-energy modes are always purely real in such a case. Next as γ increases, the range of the zero-energy mode gradually increases, and the range of the corresponding imaginary part also increases gradually, as shown in Fig. 3(b). When γ increases to 0.8 [see Fig. 3(c)], zero-energy modes exist in the ranges of $-2.5 < t_u < -1.8$ and $-0.9 < t_u < -0.15$. However, in the range of $-1.8 < t_u < -0.9$, the zero-energy modes split into two nonzero-energy modes, and at the same time, two nonzero-energy modes separate from the bulk states, resulting in four nonzero-energy modes in the gap. For the bulk-state energies, the imaginary part of them extends in the range of $t_u \in [-2.25, -0.525]$. Thus, with the increase of γ, the imaginary part of the bulk-state energies appears in wider ranges, accompanied by the enhancement of its magnitude. Meanwhile, the range of the zero-energy modes is divided. To sum up, we can understand that the nonreciprocal coupling parameter γ has a significant regulatory effect on the appearance of zero-energy modes and the bulk-state energies.

To further understand the zero-energy and nonzero-energy modes shown in Fig. 3, in Figs. 4(a)–4(d) we present the eigenenergy spectra and wave function probability density distribution of four cases, i.e., $t_u = -2.0$, $t_u = -1.5$, $t_u =$ -1.35, and $t_u = 1.0$, respectively. Relevant parameters are the same as those in Fig. 3(c). In Fig. 4(a), we see that fourfold zero-energy modes exist in the gap of this system. From the wave function probability density distribution, we can also find that the doubly degenerate zero-energy modes are localized at the left end (black line). The bulk states tend to be localized on the two sides of the chain, which can be exactly described as the non-Hermitian skin effect (green line). For the case of $t_u = -1.5$ [see Fig. 4(b)], it can be seen from the eigenenergy spectra that there are four nonzero-energy modes in the gap, and the newly generated nonzero-energy modes have no imaginary part of energy. It can be seen in Fig. 3 that this result should be attributed to the splitting of the zero-energy modes and the entrance of the bulk states into the gap. The wave function spectra Fig. 4(b) (i) and (ii) correspond to the cases of $E = \pm 0.3346$ and $E = \pm 0.1034$, respectively. Although the four nonzero-energy modes also have a tendency to be localized on the left side of the system, the wave functions show the exponential decay trend. The local effect of bulk states is also similar to that in Fig. 4(a). On the other hand, in Fig. 4(c) when $t_u = -1.35$, the four nonzero-energy modes merge in pairs, resulting in the formation of doubly degenerate nonzero-energy modes. At this time, the eigenenergies of the isolated state are $E = \pm 0.2086 \pm 0.0304i$, and the imaginary part of the eigenenergies appears. It can be observed from the wave function result that the local effect of the nonzero-energy modes is very weak at this time, whereas the bulk states mainly display the trend of localization on the right side of the system. In Fig. 4(d), it is shown that in the case of $t_u = 1.0$, the system has no zero-energy modes and is located in the topologically trivial region. From the probability density distribution of the wave function, it can be found that the bulk band states are localized at the the range of $j = 2N_u$ and $j = 2(N_u + N_d)$. The system has exhibited the non-Hermitian skin effect. Based on the above results,
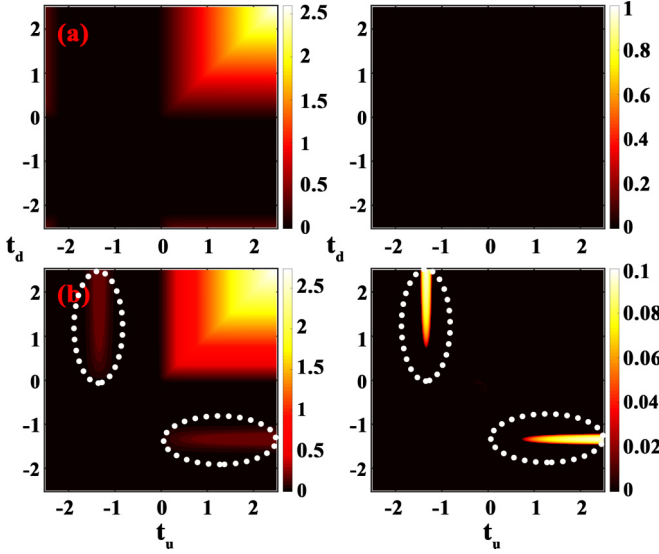
FIG. 5. Absolute-value minimum of $\mathrm{Re}(E)$ (left column) and $\mathrm{Im}(E)$ (right column) in the t_u-t_d parameter plane, where (a) $\gamma = 0.1$, and (b) $\gamma = 0.8$. Other parameters are chosen to be $N_u = N_d = 20$ and $t_2 = t_3 = 1.0$.

we know that the zero-energy modes on the topologically nontrivial region are all doubly degenerate, and the bulk states exhibit the characteristics of the non-Hermitian skin effect.

The results in Figs. 3 and 4 suggest that when $t_d = 0.8$, doubly degenerate zero-energy modes are allowed to exist in the gap. With the help of $|E|^2 = [\mathrm{Re}(E)]^2 + [\mathrm{Im}(E)]^2$, we know that if $\mathrm{Re}(E) = 0$ and $\mathrm{Im}(E) = 0$, zero-energy modes will emerge. Nevertheless if $\mathrm{Re}(E) = 0$ but $\mathrm{Im}(E) \neq 0$, purely imaginary energy modes will be induced. Next, if $\mathrm{Re}(E) \neq 0$ and $\mathrm{Im}(E) \neq 0$, there will be no zero-energy modes in the gap. In this way, the parameter space of the zero-energy modes can be well judged.

In Fig. 5, we plot the absolute-minimum phase diagram of $\mathrm{Re}(E)$ and $\mathrm{Im}(E)$ on the parameter plane formed by the change of t_u and t_d. Relevant parameters are the same as those in Fig. 3. Figure 5(a) shows the case of $\gamma = 0.1$. It can be found that the parameter range for the zero-energy modes is $t_u \in [-1.95, -0.25]$ with $t_d \in [-1.95, -0.25]$, whereas the other ranges correspond to the nonzero-energy case; namely, they belong to the bulk states. With the increase of γ, it expands the parameter range for the zero-energy modes. Besides, the imaginary-part spectra of zero-energy modes are still zero. When γ is further increased, the parameter range for the zero-energy mode becomes more complicate. Taking the case of $\gamma = 0.8$ as an example, in Fig. 5(b) we see that compared with the first case, the range of zero-energy modes is reduced, and the reduced range has been framed by the white dotted line in the figure. According to the previous conclusions, the nonzero-energy ranges in the white dotted rings are caused by the nonzero-energy modes generated by splitting of zero-energy modes. In addition, the real-part range framed by the white dotted ring is larger than the yellow range of the imaginary part. This means that the eigenenergy of the newly emerged isolated state is partly purely real and partly complex. For instance, in the case of $t_d = 0.8$, the eigenenergy
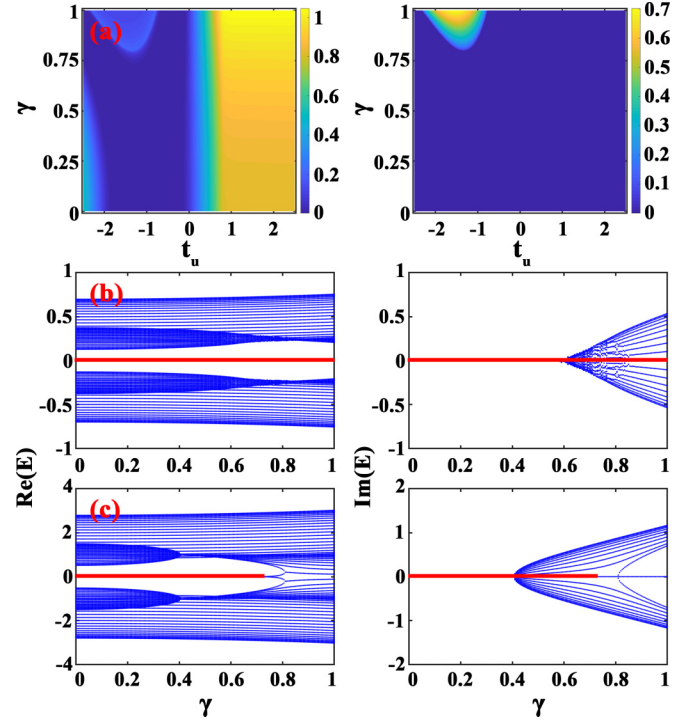

FIG. 6. (a) Absolute value minimum of $\mathrm{Re}(E)$ (left column) and $\mathrm{Im}(E)$ (right column) in the t_u-γ parameter plane. (b), (c) Band diagram with the variation of γ. The parameters are chosen as (b) $t_u = -0.5$, (c) $t_u = -1.5$. Other parameters are taken to be $N_u = N_d = 20$ and $t_2 = t_3 = 1.0$. The red (bold) lines mark the real and imaginary parts of the zero-energy modes.

of this state in $t_u \in [-1.8, -1.375]$ is real, and its complex eigenenergy occurs in the range of $t_u \in [-1.375, -1.3]$. It can be understood from the above results that γ induces nonzero-energy modes with complex energies in this system, as well as new doubly degenerate zero-energy modes.

Figure 6 shows the phase diagram of the absolute minimum values of $\mathrm{Re}(E)$ and $\mathrm{Im}(E)$ on the γ-t_u parameter plane, and the energy band with the change of γ when t_u is equal to -0.5 and -1.5, respectively. From the phase diagram [see Fig. 6(a)], we find that in the presence of finite γ, the range of zero-energy modes gradually increases; that is, the dark-blue range in the figure becomes wider. Until $\gamma = 0.7$, nonzero-energy modes begin to appear at $t_u = -1.1$. As γ continues to increase, the range of nonzero-energy modes increases, whereas the range of zero-energy modes decreases gradually. According to the energy band results above, there are nonzero-energy modes in the gap in such a case. When γ is further increased gradually, the zero-energy modes transform into the complex-eigenenergy states, and at this time, it transforms into the doubly degenerate complex-energy modes in the band gap. For example, in Fig. 6(b) where $t_u = -0.5$, we see that degenerated zero-energy modes always exist in the gap. Alternatively, in the case of $t_u = -1.5$, in Fig. 6(c) it is shown that there are doubly degenerate zero-energy modes in the gap in the region of $\gamma \leqslant 0.73$. Thereafter, the zero-energy modes and the bulk states split into four nonzero-energy modes. When $\gamma = 0.81$, they merge into two complex-energy modes with a finite imaginary part of the energy.
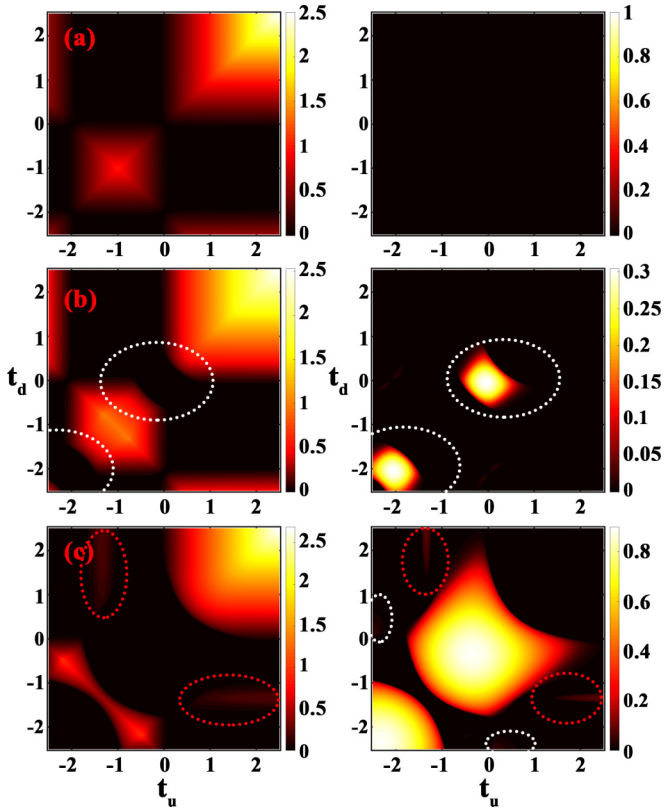
FIG. 7. Absolute value minimum of Re(E) (left column) and Im(E) (right column) in the t_u-t_d parameter plane, where (a) $\gamma = 0$, (b) $\gamma = 0.3$, and (c) $\gamma = 0.8$, respectively. Other parameters are taken to be $N_u = N_d = 20$ and $t_2 = t_3 = t_4 = 1.0$.

Up to now, we can sum up the influences of the nonreciprocal coupling parameter γ on the band structure of the coupled nonreciprocal SSH-chain configuration: (1) Introducing γ makes the system become a nonreciprocal structure, and the complex energies appear in the system. Meanwhile, the larger γ certainly leads to the enhancement of the imaginary part of energies. (2) γ can induce the transition from the topologically trivial to topologically nontrivial phase, resulting in doubly degenerate zero-energy modes in the energy gap. (3) When γ reaches its critical value, the doubly degenerate zero-energy modes will be modified and then transformed into the nonzero-energy modes.

B. Ring configuration ($t_3 \neq 0$ and $t_4 \neq 0$)

In this subsection, we continue to discuss the ring configuration in which $t_3 \neq 0$ and $t_4 \neq 0$. In order to study the effect of the degree of nonreciprocity on the zero-energy modes, in Fig. 7 we plot the phase diagrams of the minimum values of Re(E) and Im(E) on the t_u-t_d parameter plane under different γ. In this figure, the black region corresponds to Re(E) = 0 or Im(E) = 0, whereas other regions correspond to Re(E) $\neq$ 0 or Im(E) $\neq$ 0. We can readily observe that the change of γ also has a significant effect on the band structure of the ring configuration. For the result in Fig. 7(a), it describes the Hermitian case (reciprocity) where $\gamma = 0$. One can find that similarly to the chain configuration, there are still real zero energies. However, the difference consists in that when t_u and t_d
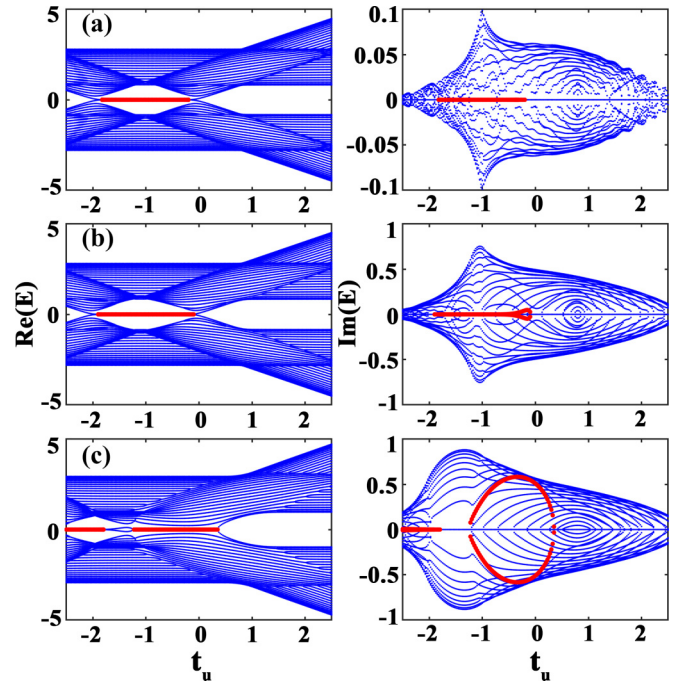

FIG. 8. Spectra of eigenenergy of our system as functions of t_u, where (a) $\gamma = 0.1$, (b) $\gamma = 0.3$, and (c) $\gamma = 0.8$. The left column is the real part of energy, and the right column is the corresponding imaginary part. The red (bold) lines correspond to the real and imaginary parts of the zero-energy and purely imaginary energy modes. The other parameters are $N_u = N_d = 20$, $t_2 = t_3 = 1.0$, $t_d = 0.8$, and $t_4 = 1.0$.

are in the range of $[-1.8, -0.2]$ simultaneously, it is no longer zero energy, which leads to the decrease of the zero-energy region compared with the chain configuration. In the presence of γ, the parameter range of zero-energy modes undergoes changes. When $\gamma = 0.3$, the parameter range of zero-energy modes is larger than the Hermitian case [new zero-energy region is marked by the white dotted line in Fig. 7(b)]. From the phase spectra of the imaginary part, it can be observed that the region of Re(E) = 0 but $|E| \neq 0$, framed by the white dashed line, indicates that these new zero-energy modes are purely imaginary energy modes. With the increase of γ, the purely imaginary energy region (white dashed line) is further extended, and gradually occupies the region of zero-energy modes in the original system. With the further increase of γ, e.g., $\gamma = 0.8$, we find that the region of nonzero-energy modes appears, as shown in the red (dotted) circle in Fig. 7(c). Like the chain configuration, this part corresponds to the purely real nonzero and complex eigenenergy modes, respectively. Therefore, with the appearance of γ, the topologically trivial and nontrivial regions in the system can be induced to display purely imaginary energy modes, and the larger γ is more helpful to enlarge the region where purely imaginary energy modes exist. The nonreciprocal strength plays its more abundant role in regulating the zero-energy modes of the ring configuration. To study the influence of nonreciprocity degree of the system on the energy spectra more specifically, Fig. 8 shows the real and imaginary energy spectra of t_u for different γ at $t_d = 0.8$. We find that for the bulk states, they always have the imaginary part of energy, which is different from the chain
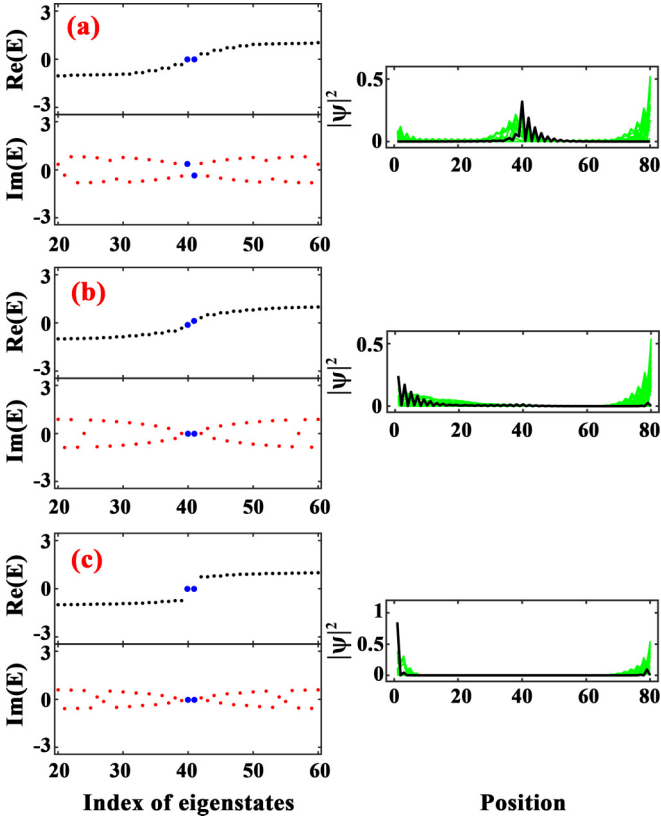
FIG. 9. Eigenenergy spectra and probability density spectra. The parameters are (a) $t_u = -1.0$, (b) $t_u = -1.4$, and (c) $t_u = -2.0$. The black (bold) lines represent the probability distribution of the zero-energy modes or nonzero-energy modes produced after splitting. Other parameters are $N_u = N_d = 20$, $t_d = 0.8$, $\gamma = 0.8$, and $t_2 = t_3 = t_4 = 1.0$.

configuration, and the maximum value of the imaginary part $\text{Im}(E)_{\text{max}} = \gamma$. For the zero-energy modes, as γ increases, the region of real part of energy gradually increases. However, the imaginary energy spectra have different phenomena with the increase of γ. When $\gamma < 0.25$, similar to the chain configuration, the imaginary part of the zero-energy mode is always zero. For the case of $\gamma > 0.25$, the imaginary part of the zero-energy state begins to appear at the position where t_u is close to zero, and the range of the imaginary part gradually increases with the increase of γ. The phenomena indicate that the purely imaginary energy modes appear in the system. The above specific results are shown in Figs. 8(a) and 8(b). Next when γ increases to 0.8, in Fig. 8(c) we find that between $t_u = -1.75$ and $t_u = -1.25$, the zero-energy modes split into two isolated states. In the range of $t_u \in [-1.25, 0.35]$, they appear as the purely imaginary energy modes, and in the range of $t_u \in [-2.5, -1.75]$ they transit from the purely imaginary energy modes to the zero-energy modes. The above results show that γ can induce the appearance of complex eigenenergies and zero-energy modes with purely imaginary energy, as well as the transition from topologically trivial regions to topologically nontrivial regions.

Similarly to the chain configuration, to better determine the characteristics of the zero-energy modes and the bulk states, in Figs. 9(a)–9(c) we present the eigenenergy spectra

and wave function probability density distribution at $t_u = -1.0$, $t_u = -1.4$, and $t_u = -2.0$, respectively. The black line in the probability density of the wave function represents the probability distribution of the zero-energy and nonzero-energy modes. For $t_u = -1.0$ in Fig. 9(a), the eigenenergies of the two purely imaginary energy modes in the gap are $E = 0 \pm 0.326i$. From the probability distribution of the wave function, we can observe that the wave function of the purely imaginary energy modes are mainly localized near $j = 2N_u$, showing an exponential decay trend along the direction of $j = 2(N_u + N_d)$. For the bulk states, most of them are localized at $j = 2N_u$ and $j = 2(N_u + N_d)$. Figure 9(b) shows the energy spectra and probability density of $t_u = -1.4$. According to the previous results, the zero-energy modes are split into nonzero-energy modes, and the two nonzero-energy modes present purely real eigenenergies. The right-side probability density spectrum corresponds to the wave function distributions of $E = \pm 0.1085$. One can see that the nonzero-energy modes exhibit the skin effect localized at $j = 1$, but the locality is very weak. For $t_u = -2.0$ in Fig. 9(c), the existence of degenerate zero-energy modes in the gap can be observed from the eigenenergy spectra. From the probability distribution of the wave function, it can also be observed that the degenerate zero-energy modes exhibit the obvious skin effect; that is, the localization is at $j = 1$. For bulk states, it also shows a trend of localization around $j = 1$ or $j = 2(N_u + N_d)$, which also satisfies the skin effect.

Through the analysis of the energy band structure and probability density of different regions, we have gotten a better understanding of the characteristics of the zero-energy modes and the bulk states. There are two types of zero-energy modes in the system: Doubly degenerate zero-energy modes with skin effect and two purely imaginary energy modes. At the same time, due to zero-energy splitting, two nonzero-energy modes with skin effect tend to be generated. From the above results, it can be seen that γ induces complex-energy spectra and zero-energy modes. In order to explore the driving effect of the γ-contributed nonreciprocity degree on the energy spectra, we plot the phase diagram of the minimum values of $\text{Re}(E)$ and $\text{Im}(E)$ on the t_u-γ plane, as well as the energy-band spectra in the real space following the variation of γ. From Figs. 10(a)–10(c), we find that for the case of $\gamma \in [0, 0.25]$, the range of zero-energy modes increases gradually with the increase of γ [i.e., phase II in Fig. 10(c)]. The other regions are located in the topologically trivial phase [phase I in Fig. 10(c)]. Until $\gamma = 0.25$, the purely imaginary energy modes appear in the gap [phase III in Fig. 10(c)], and the range also increases gradually as γ increases. In addition, we also observe that when γ is increased to 0.73, the nonzero-energy modes [phase IV in Fig. 10(c)] appear in the gap, which is generated by zero-energy mode splitting. Complex-energy eigenstates [phase V in Fig. 10(c)] begin to appear in the gap when $\gamma > 0.81$. During this process, the range of zero-energy modes gradually decreases. Figures 10(d)–10(f) show the band structures in the case of $t_u = -1.0$, $t_u = -1.5$, and $t_u = -2.1$, respectively. It can be found that when $t_u = -1.0$, with the increase of γ, there are first the doubly degenerate zero-energy modes and then two purely imaginary energy modes in the gap. For $t_u = -1.5$, the real zero-energy modes always exist in the range of $\gamma < 0.74$, and then split into
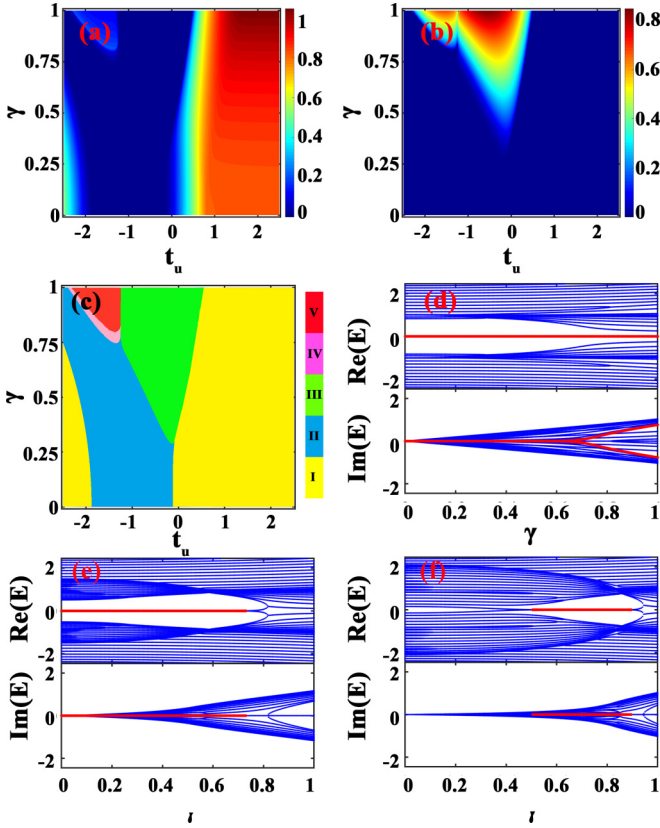
FIG. 10. (a), (b) Absolute-value minimum of Re(E) (left column) and Im(E) (right column) in the t_u-γ parameter plane. (c) The phase diagram of the modes in the gap. (d)–(f) Band diagrams with the change of γ. The parameters are (d) $t_u = -1.0$, (e) $t_u = -1.5$, and (f) $t_u = -2.1$. Red (bold) lines mark the real and imaginary parts of zero-energy modes. Relevant parameters are set as $N_u = N_d = 20$ and $t_2 = t_3 = t_4 = 1.0$.

the nonzero-energy modes in the following. As γ increases to 0.81, they are converted to complex-energy modes. In the case of $t_u = -2.1$, it can be observed that the system transits from topologically trivial to topologically nontrivial phase following the change of γ, and accordingly, the doubly degenerate zero-energy modes appear in the gap. Likewise, when γ increases to 0.9, the zero-energy mode splitting comes into being.

Based on the above results, we would like to summarize the regulation effect of γ on the energy spectrum of our considered ring configuration: (1) It induces the splitting of the zero-energy modes to form the nonzero-energy modes. (2) It enhances the transition from the topologically trivial to topologically nontrivial phase, accompanied by the appearance of the doubly degenerate zero-energy modes in the gap. (3) It promotes the doubly degenerate zero-energy modes in the topologically nontrivial region to transform into two purely imaginary energy modes.

C. Roles of disorder

It is known that disorders usually play nontrivial roles in modifying the band structures of quantum systems. In view of this fact, in Fig. 11 we explore the changes of the
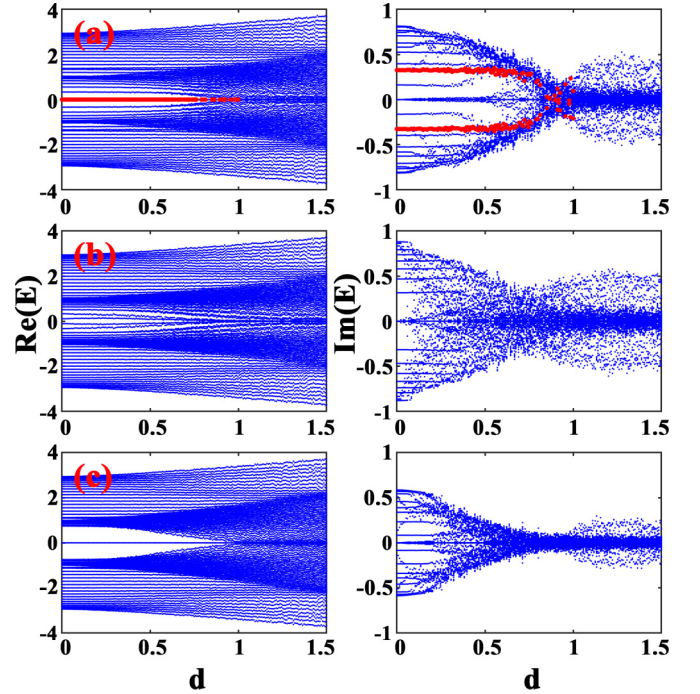

FIG. 11. (a)–(c) Energy spectra influenced by the different-strength disorder. The spectra are the average over 100 disorder results. In (a)–(c), the disorder is applied according to the manner of $t_2' = t_2 + dw_n$ with $w_n \in [-1.0, 1.0]$ and d being the disorder parameter. The parameters are set as (a) $t_u = -1.0$, (b) $t_u = -1.4$, and (c) $t_u = -2.0$. The other parameters are $t_2 = t_3 = t_4 = 1.0$ and $N_u = N_d = 20$.

eigenenergy spectra due to the presence of disorders. Our main purpose is to clarify the robustness of edge states and skin effects to disorders. According to the previous works, the robustness to disorders is a very important property of edge states. Therefore, we numerically investigate the robustness of edge states and skin effects to disorders, by taking the ring configuration as an example. In this work, we consider the case of off-diagonal disorder, by introducing the disorder in the intercell hopping terms, that is, $t_2' = t_2 + dw_n$, where n is the cell index, w_n is uniformly distributed between -1.0 and 1.0, and d is the disorder strength. Figure 11 presents the energy spectra influenced by the increase of disorder strength d, in the ring configuration. Figures 11(a)–11(c) correspond to the purely imaginary energy modes, nonzero-energy modes, and doubly degenerate zero-energy modes of Figs. 9(a)–9(c), respectively. For the bulk states, their bands are widened following the increase of disorder strength d. However, the isolated modes undergo different changes in this process. It can be observed in Fig. 11(a) that for two purely imaginary energy modes, when $d < 0.6$, they are robust to weak disorder even though the details of imaginary part are modified. In comparison, the four isolated modes are not robust to disorder and integrate into the bulk bands as the disorder strength d increases. Next, regarding the doubly degenerate zero-energy modes, they have better robustness to weak disorder. During the increase of the disorder strength, the widening of the bulk bands causes these modes to be merged. Therefore, we can conclude that both purely imaginary energy modes and doubly
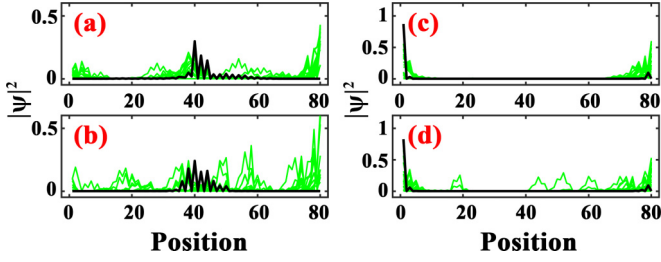
FIG. 12. Probability density spectra with the different strengths of disorder, when $t_u = -1.0$ [(a), (b)] and $t_u = -2.0$ [(c), (d)]. The strength of disorder is taken to be (a), (c) $d = 0.4$, and (b), (d) $d = 0.8$, respectively. Other parameters are $t_2 = t_3 = t_4 = 1.0$ and $N_u = N_d = 20$. The spectra are the average over 100 disorder results.
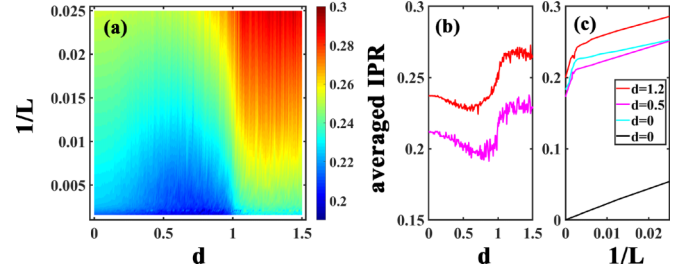

FIG. 13. (a) Phase diagram for the $\overline{\text{IPR}}$ with the change of d and $1/L$. (b) Red (upper) and pink (lower) lines represent the $\overline{\text{IPR}}$ of $L = 80$ and $L = 640$, respectively. (c) The red (first), pink (second) and light blue (third) lines denote the $\overline{\text{IPR}}$ of $d = 1.2$, $d = 0.5$, and $d = 0$, respectively, when $\gamma = 0.8$. The black (bottom) line is the $\overline{\text{IPR}}$ of $d = 0$ when $\gamma = 0$. Other parameters are $t_2 = t_3 = t_4 = 1.0$. The spectra are the average over 100 disorder results.

degenerate zero-energy modes are robust to weak disorder, whereas the degenerate zero-energy modes are more robust in comparison. This provides new content for identifying the isolated modes in the gap.

In order to study the effect of disorder on non-Hermitian skin effect and edge states, we present the probability density of the wave function of the ring configuration for different strengths of disorder. Figures 12(a) and 12(b) correspond to the probability density of the case of $t_u = -1.0$ with $\gamma = 0.8$. From Fig. 9(a), we know that two purely imaginary energy modes exist in the gap and the wave function of the purely imaginary energy modes are mainly localized near $j = 2N_u$. For such purely imaginary modes, from the black (bold) lines, we can find that as γ increases, the locality of the wave function can be affected. For example, when $d = 0.4$, the wave function is still mainly localized around $j = 40$, with exhibiting the exponential decay near $j > 40$. However, when $d = 0.8$, the locality effect of the wave function is destroyed obviously. This result indicates that disorder has a certain negative effect on the skin effect of the purely imaginary energy modes. Regarding the bulk states, the disorder destroys the non-Hermitian skin effects as well. With the enhancement of disorder, the wave function of the bulk states gradually shows the tendency to spread along the SSH lattice. Figures 12(c) and 12(d) show the probability density of bulk states and zero-energy modes at $t_u = -2.0$. From Fig. 9(c), the system has two degenerate zero-energy modes which are localized on the left side for $d = 0$. With the increase of the strength d, it can be observed that although the trend of probability density of bulk states is similar to the result of $t_u = -1.0$, the zero-energy modes are still localized on the beginning side, which seems to be independent of disorder. This exactly suggests that the zero-energy modes are robust to weak disorder. Based on the above results, we can find that disorder has a serious damage to the skin effect of bulk states. This also makes it easier to better distinguish between purely imaginary energy modes and the zero-energy modes.

Finally, we would like to introduce the averaged inverse participation rate ($\overline{\text{IPR}}$), for the sake of presenting the detailed analysis about the effect of disorder on the locality of wave functions. According to the previous works [44,47,48], it is defined as

$$\overline{\text{IPR}} = \frac{1}{L} \sum_{n=1}^{L} \text{IPR}_n = \frac{1}{L} \sum_{n=1}^{L} \frac{1}{\text{PR}_n}$$

$$= \frac{1}{L} \sum_{n=1}^{L} \frac{\sum_l |\Psi_n(l)|^4}{\sum_l |\Psi_n(l)|^2}, \tag{24}$$

where IPR_n (PR_n) is the inverse participation rate (participation rate) and Ψ_n is the nth right eigenvector of H [44,47–53]. L is the size of the considered system. For Hermitian or non-Hermitian systems, IPR_n (PR_n) is often used to determine the locality of Ψ_n. It is known that for extended states, $\text{IPR}_n \simeq 1/L$ and tends to be equal to zero as $L \to \infty$. On the other hand, the inverse participation rate of the localized states will tend to be a nonzero and finite value with the increase of the system's size, i.e., L. Accordingly, it has been found that $\text{IPR}_n = 1$ ($\text{PR}_n = 1$) for the completely localized states [49–51]. Such theories have also been applied to the systems with disorders [50,51].

Following the above theory, in Fig. 13 we present the $\overline{\text{IPR}}$ of the ring configuration by considering the different parameters. From this figure, we find that for a certain length L ($L = 2N_u + 2N_d$), the value of $\overline{\text{IPR}}$ shows the nonlinear change behavior following the increase of the disorder strength. First, in the presence of weak disorder, increasing the disorder strength leads to a gradual decrease of $\overline{\text{IPR}}$. This directly means the weakening of the localization of the respective states involved. When disorder continues increasing, the values of $\overline{\text{IPR}}$ for strong disorder have a significant upward trend compared with those in the weak-disorder region. As shown by the case of $L = 80$ in Fig. 13(b), $\overline{\text{IPR}}$ decreases from 0.237 to 0.224 as the strength of disorder increases to $d = 0.72$. Alternatively, when d further increases, $\overline{\text{IPR}}$ is gradually enhanced to 2.7. Next, the result of $L = 640$ displays the similar phenomenon [see the pink line in Fig. 13(b)]. In addition, it can be observed that the size increase of the SSH lattice is inversely proportional to the growth of the value of $\overline{\text{IPR}}$. With the increment of the lattice size, $\overline{\text{IPR}}$ gradually decreases to its nonzero value at the same disorder strength. In Fig. 13(c), we plot the relationship between $\overline{\text{IPR}}$ and $1/L$. It is shown that for the case of $\gamma = 0.8$, with the increase of L, $\overline{\text{IPR}}$ gradually arrives at 0.2 when $d = 1.2$. According to the previous theoretical conclusion, it can be seen that the localization of the respective states does not disappear with the increase of the lattice size. In comparison, when $d = 0$ and $\gamma = 0$ (the black

line), $\overline{\text{IPR}}$ gradually approaches 0 when $L \to \infty$, which exactly corresponds to the description of extended states. This is consistent with the theoretical results. Therefore, by analyzing the averaged inverse participation rate, the regulatory effect of disorder on the locality of the different states can be further understood.

According to the disorder results, we can make the following conclusion, especially for the band structures and skin effect: (1) For the isolated modes, the degenerate zero-energy modes are more robust in comparison with others. (2) Disorder can regulate the skin effects of the isolated modes and bulk states. Compared with the isolated modes, the skin effect of the bulk states suffers from more negative influence of disorder.

IV. SUMMARY

In summary, we have constructed the SSH lattice with domain wall boundary conditions and introduced the nonreciprocal coupling parameter γ to this coupled structure, to clarify the band variations and skin effects. After exploring its influence on the band structures of chain and ring configurations, we have found that the nonreciprocal coupling plays its nontrivial role in governing the non-Hermitian skin effect for both configurations. To be specific, it widens the parameter space of the zero-energy modes, and modifies the transition manner from topologically trivial to topologically nontrivial phase. When the nonreciprocal coupling is increased to its critical value, the zero-energy modes will be separated from each other, and then new nonzero- or complex-energy modes will be allowed to appear in the band gap. What is more, differently from the chain configuration, the nonreciprocal coupling makes purely imaginary energy modes arise in the band gap of the SSH-ring configuration. All these results suggest the nontrivial effect of nonreciprocal mechanism on the band structure and edge states of our considered SSH lattice. On the other hand, if intercell-hopping disorder is incorporated, it shows that the zero-energy modes are more robust than the other modes, whereas the imaginary part of energies undergoes the nonmonotonic changes. Based on the numerical results, we believe that this work is helpful in understanding the influences of nonreciprocal couplings on the types and properties of isolated modes in the SSH lattices.

APPENDIX: TOPOLOGICAL PHASE CONDITION IN SINGLE NON-HERMITIAN SSH CHAIN

In the following, we would like to check the case of the single non-Hermitian SSH chain, with the help of theory in Sec. II. Accordingly, the structural parameters can considered to be $t_3 = t_4 = 0$, $t_\alpha = \tilde{t}$, and $N_\alpha = N$; meanwhile, Ψ can be

written as $\Psi = (\psi_{a,1}, \psi_{b,1}, \ldots, \psi_{a,N}, \psi_{b,N})^T$. It can be readily found that the eigenvalue equations should also be simplified, including the bulk equations and boundary equations:

$$(\tilde{t} + t_0 e^{-\gamma})\psi_{b,n} + t_2 \psi_{b,n-1} = E\psi_{a,n}, \quad (A1)$$

$$(\tilde{t} + t_0 e^{\gamma})\psi_{a,n} + t_2 \psi_{a,n+1} = E\psi_{b,n}, \quad (A2)$$

$$(\tilde{t} + t_0 e^{-\gamma})\psi_{b,1} = E\psi_{a,1}, \quad (A3)$$

$$(\tilde{t} + t_0 e^{\gamma})\psi_{a,N} = E\psi_{b,N}. \quad (A4)$$

According to Eq. (8), $\psi_{a,n}$ and $\psi_{b,n}$ satisfy $\psi_{a(b),n} = \sum_1^2 \beta_j^n \phi_{a(b)}^j = \beta_1^n \phi_{a(b)}^1 + \beta_2^n \phi_{a(b)}^2$. Together with Eqs. (A1) and (A2), they lead to $[(\tilde{t} + t_0 e^{-\gamma}) + t_2 \beta_j^{-1}]\phi_b^j = E\phi_a^j$ and $[(\tilde{t} + t_0 e^{\gamma}) + t_2 \beta_j]\phi_a^j = E\phi_b^j$. Therefore, we can get the characteristic equation of the non-Hermitian SSH chain, i.e.,

$$t_2(\tilde{t} + t_0 e^{-\gamma})\beta_j + t_2(\tilde{t} + t_0 e^{\gamma})\frac{1}{\beta_j}$$
$$+ [\tilde{t}^2 + 2\tilde{t}t_0 \cosh(\gamma) + t_0^2 + t_2^2] = E^2. \quad (A5)$$

Its two solutions are $\beta_{1(2)} = \{-x + (-)\sqrt{x^2 - 4t_2^2[\tilde{t}^2 + 2\tilde{t}t_0 \cosh(\gamma) + t_0^2]}\}/[2t_2(\tilde{t} + t_0 e^{-\gamma})]$, where $x = \tilde{t}^2 + 2\tilde{t}t_0 \cosh(\gamma) + t_0^2 + t_2^2 - E^2$ with $\beta_1 \beta_2 = \frac{\tilde{t} + t_0 e^{\gamma}}{\tilde{t} + t_0 e^{-\gamma}}$. At the limit of $E \to 0$, the expressions of β_1 and β_2 are approximated as

$$\beta_1|_{E \to 0} = -\frac{\tilde{t} + t_0 e^{\gamma}}{t_2}, \quad \beta_2|_{E \to 0} = -\frac{t_2}{\tilde{t} + t_0 e^{-\gamma}}. \quad (A6)$$

Substituting Eq. (10) into Eqs. (A3) and (A4), we get

$$\beta_1^{N+1}[(\tilde{t} + t_0 e^{\gamma}) + t_2 \beta_2] = \beta_2^{N+1}[(\tilde{t} + t_0 e^{\gamma}) + t_2 \beta_1]. \quad (A7)$$

In the situation of $N \to \infty$, the condition for Eq. (A7) is $|\beta_1| = |\beta_2|$, for the bulk states. Together with $\beta_1 \beta_2 = \frac{\tilde{t} + t_0 e^{\gamma}}{\tilde{t} + t_0 e^{-\gamma}}$, they lead to $|\beta_j| = \sqrt{|\frac{\tilde{t} + t_0 e^{\gamma}}{\tilde{t} + t_0 e^{-\gamma}}|}$. When the parametric relationship satisfies $|\beta_j(E \to 0)| = r$, the open-boundary continuum will reach zero energy. And then, we have

$$\tilde{t} = -t_0 \cosh(\gamma) \pm \sqrt{t_0^2 \cosh^2(\gamma) - t_0^2 + t_2^2}, \quad (A8)$$

or

$$\tilde{t} = -t_0 \cosh(\gamma) \pm \sqrt{t_0^2 \cosh^2(\gamma) - t_0^2 - t_2^2}. \quad (A9)$$

They exactly describe the critical positions of the topological phase transition. According to the relation of β, we set $\beta = re^{ik}$, where $r = \sqrt{|\tilde{t} + t_0^2 e^{\gamma}/\tilde{t} + t_0 e^{-\gamma}|}$ and $k \in [0, 2\pi]$. Together with the characteristic equation, we get

$$E^2(k) = \tilde{t}^2 + 2\tilde{t}t_0 \cosh(\gamma) + t_2\sqrt{(\tilde{t} + t_0 e^{\gamma})(\tilde{t} + t_0 e^{-\gamma})}$$
$$[\text{sgn}(\tilde{t} + t_0 e^{-\gamma})e^{ik} + \text{sgn}(\tilde{t} + t_0 e^{\gamma})e^{-ik}] + t_0^2 + t_2^2. \quad (A10)$$

When $\tilde{t}$ satisfies the condition that $-t_0 \cosh(\gamma) - t_0\sqrt{\cosh^2(\gamma) - 1} < \tilde{t} < -t_0 \cosh(\gamma) + t_0\sqrt{\cosh^2(\gamma) - 1}$, the system has the complex eigenenergies, whereas in the other regions the eigenenergies are real.

[1] R. Shankar, *Princples of Quantum Mechanics* (Springer, New York, 1994).

[2] B. G. Zhu, R. Lü, and S. Chen, Phys. Rev. A **89**, 062102 (2014).

[3] L. Fu, C. L. Kane, and E. J. Mele, Phys. Rev. Lett. **98**, 106803 (2007).

[4] Z. J. Chen and X. J. Ning, Acta Phys. Sin. **52**, 2683 (2003).

[5] C. M. Bender and S. Boettcher, Phys. Rev. Lett. **80**, 5243 (1998).

[6] C. M. Bender, Rep. Prog. Phys. **70**, 947 (2007).

[7] C. M. Bender, D. C. Brody, and H. F. Jones, Phys. Rev. Lett. **89**, 270401 (2002).

[8] S. Longhi, Phys. Rev. A **88**, 052102 (2013).

[9] F. K. Kunst, E. Edvardsson, J. C. Budich, and E. J. Bergholtz, Phys. Rev. Lett. **121**, 026808 (2018).

[10] L. Jin, P. Wang, and Z. Song, Sci. Rep. **7**, 5903 (2017).

[11] Y. Xing, L. Qi, J. Cao, D. Y. Wang, C. H. Bai, H. F. Wang, A. D. Zhu, and S. Zhang, Phys. Rev. A **96**, 043810 (2017).

[12] X. S. Li, Z. Z. Li, L. L. Zhang, and W. J. Gong, J. Phys.: Condens. Matter **32**, 165401 (2020).

[13] K. Kawabata, Y. Ashida, H. Katsura, and M. Ueda, Phys. Rev. B **98**, 085116 (2018).

[14] M. Klett, H. Cartarius, D. Dast, J. Main, and G. Wunner, Phys. Rev. A **95**, 053626 (2017).

[15] L. Jin, Phys. Rev. A **96**, 032103 (2017).

[16] L. L. Zhang, J. R. Li, D. Zhang, T. T. Xu, W. B. Cui, and W. J. Gong, Results Phys. **34**, 105274 (2022).

[17] X. M. Zhao, C. X. Guo, S. P. Kou, L. Zhuang, and W. M. Liu, Phys. Rev. B **104**, 205131 (2021).

[18] C. Yuce and H. Ramezani, Phys. Rev. A **100**, 032102 (2019).

[19] L. Feng, R. El-Ganainy, and L. Ge, Nat. Photonics **11**, 752 (2017).

[20] A. Regensburger, C. Bersch, M. A. Miri, G. Onishchukov, D. N. Christodoulides, and U. Peschel, Nature (London) **488**, 167 (2012).

[21] L. Lu, J. D. Joannopoulos, and M. Soljăcić, Nat. Photonics **8**, 821 (2014).

[22] M. G. Silveirinha, Phys. Rev. B **99**, 125155 (2019).

[23] T. Ozawa, H. M. Price, A. Amo, N. Goldman, M. Hafezi, L. Lu, M. C. Rechtsman, D. Schuster, J. Simon, O. Zilberberg, and I. Carusotto, Rev. Mod. Phys. **91**, 015006 (2019).

[24] H. Hodaei, M. A. Miri, A. U. Hassan, W. E. Hayenga, M. Heinrich, D. N. Christodoulides, and M. Khajavikhan, Laser Photonics Rev. **10**, 494 (2016).

[25] H. Jing, S. K. Ozdemir, X. Y. Lü, J. Zhang, L. Yang, and F. Nori, Phys. Rev. Lett. **113**, 053604 (2014).

[26] Y. D. Chong, L. Ge, and A. D. Stone, Phys. Rev. Lett. **106**, 093902 (2011).

[27] M. Kang, F. Liu, and J. Li, Phys. Rev. A **87**, 053824 (2013).

[28] Y. Sun, W. Tan, H. Q. Li, J. Li, and H. Chen, Phys. Rev. Lett. **112**, 143903 (2014).

[29] S. Yao and Z. Wang, Phys. Rev. Lett. **121**, 086803 (2018).

[30] S. Yao, F. Song, and Z. Wang, Phys. Rev. Lett. **121**, 136802 (2018).

[31] V. M. Martinez Alvarez, J. E. Barrios Vargas, and L. E. F. Foa Torres, Phys. Rev. B **97**, 121401(R) (2018).

[32] C. H. Lee and R. Thomale, Phys. Rev. B **99**, 201103(R) (2019).

[33] S. Weidemann, M. Kremer, T. Helbig, T. Hofmann, A. Stegmaier, M. Greiter, R. Thomale, and A. Szameit, Science **368**, 311 (2020).

[34] Y. Xiong, J. Phys. Commun. **2**, 035043 (2018).

[35] T. E. Lee, Phys. Rev. Lett. **116**, 133903 (2016).

[36] T. S. Deng and W. Yi, Phys. Rev. B **100**, 035102 (2019).

[37] F. Song, S. Yao, and Z. Wang, Phys. Rev. Lett. **123**, 246801 (2019).

[38] K. Yokomizo and S. Murakami, Phys. Rev. Lett. **123**, 066404 (2019).

[39] L. Xiao, T. S. Deng, K. K. Wang, G. Y. Zhu, Z. Wang, W. Yi, and P. Xue, Nat. Phys. **16**, 761 (2020).

[40] P. C. Cao, Y. G. Peng, Y. Li, and X. F. Zhu, Chin. Phys. Lett. **39**, 057801 (2022).

[41] A. Ghatak, M. Brandenbourger, J. van Wezel, and C. Coulais, Proc. Natl. Acad. Sci. USA **117**, 29561 (2020).

[42] E. J. Bergholtz, J. C. Budich, and F. K. Kunst, Rev. Mod. Phys. **93**, 015005 (2021).

[43] T. Helbig, T. Hofmann, S. Imhof, M. Abdelghany, T. Kiessling, L. W. Molenkamp, C. H. Lee, A. Szameit, M. Greiter, and R. Thomale, Nat. Phys. **16**, 747 (2020).

[44] C. X. Guo, C. H. Liu, X. M. Zhao, Y. Liu, and S. Chen, Phys. Rev. Lett. **127**, 116801 (2021).

[45] K. Kawabata, K. Shiozaki, M. Ueda, and M. Sato, Phys. Rev. X **9**, 041015 (2019).

[46] Z. P. Gong, Y. Ashida, K. Kawabata, K. Takasan, S. Higashikawa, and M. Ueda, Phys. Rev. X **8**, 031079 (2018).

[47] F. L. Metz and I. Neri, Phys. Rev. Lett. **126**, 040604 (2021).

[48] H. Jiang, L. J. Lang, C. Yang, S. L. Zhu, and S. Chen, Phys. Rev. B **100**, 054301 (2019).

[49] Y. X. Liu, Y. C. Wang, X. J. Liu, Q. Zhou, and S. Chen, Phys. Rev. B **103**, 014203 (2021).

[50] L. J. Zhai, G. Y. Huang, and S. Yin, Phys. Rev. B **104**, 014202 (2021).

[51] C. Mejía-Cortés and M. I. Molina, Phys. Rev. A **91**, 033815 (2015).

[52] L. Jin and Z. Song, Phys. Rev. B **99**, 081103(R) (2019).

[53] F. Evers and A. D. Mirlin, Phys. Rev. Lett. **84**, 3690 (2000).